



## RESEARCH LETTER

10.1002/2015GL067342

## Key Points:

- The lunar gravitational semidiurnal tide ( $L_2$ ) is detected in the TRMM rainfall data
- The observed phase relationship between pressure and rainfall is in accord with linear theory
- Adiabatic expansion due to  $L_2$  increases rainfall rate by 10% per 1% increase in relative humidity

## Supporting Information:

- Figure S1

## Correspondence to:

T. Kohyama,  
kohyama@uw.edu

## Citation:

Kohyama, T., and J. M. Wallace (2016), Rainfall variations induced by the lunar gravitational atmospheric tide and their implications for the relationship between tropical rainfall and humidity, *Geophys. Res. Lett.*, **43**, doi:10.1002/2015GL067342.

Received 8 DEC 2015

Accepted 4 JAN 2016

Accepted article online 7 JAN 2016

©2016. The Authors.

This is an open access article under the terms of the Creative Commons Attribution-NonCommercial-NoDerivs License, which permits use and distribution in any medium, provided the original work is properly cited, the use is non-commercial and no modifications or adaptations are made.

## Rainfall variations induced by the lunar gravitational atmospheric tide and their implications for the relationship between tropical rainfall and humidity

Tsubasa Kohyama<sup>1</sup> and John M. Wallace<sup>1</sup><sup>1</sup>Department of Atmospheric Sciences, University of Washington, Seattle, Washington, USA

**Abstract** Classical tidal theory predicts that the lunar gravitational semidiurnal tide ( $L_2$ ) should induce perturbations in relative humidity (RH). Adiabatic expansion in divergent flow in advance of the  $L_2$  pressure minimum cools the air and reduces its saturation vapor pressure, thereby increasing the rate of condensation in saturated air parcels and causing the relative humidity (RH) of unsaturated parcels to rise. Here we detect a statistically significant  $L_2$  signature in precipitation rate ( $P$ ) in a 15 year, eight times daily, global precipitation data set acquired in the Tropical Rainfall Measuring Mission. Consistent with tidal theory and with the notion that  $L_2$  modulates  $P$  mainly by perturbing RH,  $P$  varies out of phase with pressure, and it increases at a rate of about 10% per 1% increase in RH. These measurements thus provide a measure of the sensitivity of  $P$  to planetary-scale changes in RH. Analysis of solar semidiurnal ( $S_2$ ) tidal statistics yields similar results.

### 1. Introduction

Among the members of the large extended family of atmospheric perturbations, the lunar gravitational semidiurnal atmospheric tide ( $L_2$ ), the forced response to perturbations in the gravitational field occupies a special niche. It is nearly periodic and therefore easy to isolate; it is small in amplitude and therefore linear, and its forcing is simple, planetary scale, and almost perfectly known. By virtue of these special properties, the polarities and relative amplitudes of the  $L_2$  signal in different atmospheric variables shed light on more general relationships between variables such as between planetary-scale relative humidity (RH) and precipitation rate ( $P$ ) in the tropical atmosphere.

Classical tidal theory, e.g., as presented in *Lindzen and Chapman* [1969] predicts the existence of a linear relationship between perturbations in pressure and RH. *Chapman* [1951] showed that the  $L_2$  cycles in pressure and temperature are in phase, from which he deduced that the tidal temperature perturbations are induced by adiabatic compression and expansion of air parcels. In accordance with the Clausius-Clapeyron equation, saturation vapor pressure should vary in phase with temperature. Therefore, if we assume that specific humidity remains constant to first order on the semidiurnal time scale, RH should vary out of phase with temperature and pressure. The temperature perturbations affect  $P$  both directly, by cooling saturated air during the expansion phase 1/4 cycle in advance of low tide, and indirectly, by making conditions favorable for heavier  $P$  at the time of low tide, when the ambient, planetary-scale RH is highest. The phase of the  $P$  signature provides an indication of whether the direct or indirect effect is dominant. To the extent that the indirect effect dominates, the relative amplitude of the RH and  $P$  tidal signals is an indicator of the sensitivity of  $P$ , on a planetary scale, to changes in ambient, column-integrated RH.

Until recently, studies of atmospheric tides have been based exclusively on a sparse network of station data [e.g., *Haurwitz and Cowley*, 1969; *Goulter*, 2005], and a robust  $L_2$  signal has been identified only in pressure and, to a more limited extent, in temperature. In *Kohyama and Wallace* [2014] (hereafter KW14), we detected a robust lower atmospheric  $L_2$  signal in the ERA-Interim reanalysis. Our analysis was focused on the geopotential height field, but the procedure that we used could be applied to any atmospheric variable. A limitation of this approach is that estimates of ratios of  $L_2$  amplitudes in different variables are, at least to some degree, model dependent. An estimate of the sensitivity of  $P$  to ambient RH would be more convincing if the  $L_2$  signal in  $P$  could be derived independently of the ERA-Interim. Accordingly, we examine the 15 year record

of eight times daily data derived from Tropical Rainfall Measurement Mission (TRMM). As described in this paper, we detect a statistically significant  $L_2$  signal with the highest  $P$  at the time of the lowest pressure, in accordance with classical tidal theory and with the notion that the  $L_2$  signal in  $P$  is mainly a response to the RH perturbations. Hence, we are justified in using estimates of the tidal amplitudes to infer the sensitivity of  $P$  to planetary-scale perturbations in RH.

The paper is structured as follows. Data and methods used in this study are described in section 2. In section 3, we isolate  $L_2$  signals from the TRMM rainfall data. Then, in section 4, we discuss some implications for the relationship between tropical RH and  $P$ . Some concluding remarks are presented in section 5.

## 2. Data and Methods

### 2.1. Data

The  $P$  data are from TRMM Multisatellite Precipitation Analysis data [Huffman *et al.*, 2007]. This data set is augmented by including observational data from other satellite-borne microwave imagers and infrared sensors. The latitude range of the data set is 50°S to 50°N. The original horizontal resolution is 0.25° in both longitudinal and latitudinal directions, but we have regridded the data at 4° resolution for computational efficiency. The time span analyzed in this study is from 1998 to 2012 for  $P$ .

The geopotential, temperature, and horizontal divergence fields are from the four times daily ERA-Interim reanalysis produced by the European Centre for Medium-Range Weather Forecasts [Dee *et al.*, 2011]. The data are generated by a multivariate data assimilation scheme in which gridded forecast fields produced by a numerical weather prediction model are continually being updated with satellite and in situ observational data. The resulting gridded fields are reanalyzed for research use. The horizontal resolution analyzed in this study is 4.5° in both longitude and latitude for geopotential and temperature and 3.0° for horizontal divergence. The time span of the analysis is 1979–2011 for geopotential height and 1979–2014 for temperature and horizontal divergence. Geopotential height is calculated by dividing geopotential by standard gravity. These variables are analyzed after calculating the mass-weighted vertical mean for 100–1000 hPa pressure layer. Taking the mass-weighted vertical mean is justified because KW14 showed that the tidal amplitude increases linearly with height in the tropical troposphere, and only by less than 20% from the Earth's surface to the 100 hPa level.

As noted in KW14, the model used in assimilating the data lacks the forcing for the tide. Hence, the assimilation process could conceivably lead to a damping of the tidal signal in the global analyses. However, we believe that the error associated with this damping effect cannot be too large, because KW14 showed that the detected  $L_2$  pressure tidal signals are generally consistent with the  $L_2$  signals estimated by station data in earlier studies. In addition, a recent work by Schindelegger and Dobslaw [2016] has confirmed that the  $L_2$  in the ERA-Interim reanalysis shows a remarkably close agreement with the global ground truth view of the  $L_2$  estimated from land barometers and moored buoys.

### 2.2. Methods

To isolate the  $L_2$  signal from an arbitrary meteorological variable  $x$ , we first prepare for four separate daily time series  $x_{00}$ ,  $x_{06}$ ,  $x_{12}$ , and  $x_{18}$  by extracting data for each of the four analysis times (00, 06, 12, and 18 UTC, respectively) at each grid point. Then, we construct the regression maps (The formula given by KW14 is wrong by a factor of  $\sqrt{2}$ ):

$$A_i(\lambda, \phi) = \overline{2 x'_i(\lambda, \phi, t) \cos\left(\frac{2\pi}{T_s} t\right)} \quad (1)$$

$$B_i(\lambda, \phi) = \overline{2 x'_i(\lambda, \phi, t) \sin\left(\frac{2\pi}{T_s} t\right)} \quad (2)$$

where  $i = 00, 06, 12, \text{ and } 18$ ,  $\lambda$  is longitude,  $\phi$  is latitude,  $t$  is time, and  $T_s$  is half the lunar synodic period (14.765294 days). Overbars and primes denote time means and departures from them, respectively. This regression procedure is based on the fact that when repeatedly observed at a particular mean solar time each day, the Moon revolves eastward and completes a full circuit around the Earth during a full lunar synodic cycle. The reference time ( $t = 0$ ) is defined as the time of one of the full or new moons within the time span of

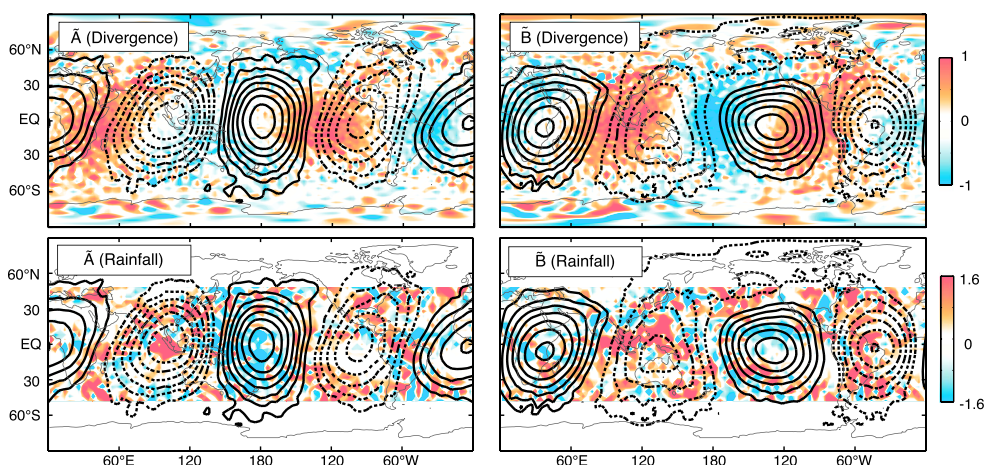


**Figure 1.** (top row) Amplitude of the lunar semidiurnal pressure tide (contours) and wind tide (shading) estimated by regressing mass-weighted vertical mean geopotential height ( $Z$ ) and horizontal divergence in the 100–1000 hPa layer upon the cosine ( $\bar{A}$ ; top left) and sine ( $\bar{B}$ ; top right) time series with a period of a half lunar synodic cycle (14.765 days), starting at the time of the new or full moon. The “weather noise” is suppressed by differencing the regression maps for the four daily analysis times using the relation (00 UTC 06 UTC + 12 UTC 18 UTC)/4. Contour interval for  $Z$  is 0.1 m, units of  $10^{-8} \text{ s}^{-1}$  for horizontal divergence. Zero contours are omitted, and negative contours are dashed. (bottom row) As in Figure 1 (top row) but for  $Z$  (contours) and precipitation rate (shading). For precipitation rate, the weather noise is suppressed by differencing the regression maps for the eight daily analysis times using the relation  $\bar{A} = (A_{00} - A_{06} + A_{12} - A_{18} + B_{03} - B_{09} + B_{15} - B_{21})/8$  and  $\bar{B} = (B_{00} - B_{06} + B_{12} - B_{18} - A_{03} + A_{09} - A_{15} + A_{21})/8$ . In units of  $\mu\text{m}/\text{h}$  for precipitation rate.

interest, so that the cosine series reaches its maxima at the times of the full and new moons and its minima at the times of the half moons. Then we calculate the differences between the regression maps with opposing phases,  $\bar{A} = (A_{00} - A_{06} + A_{12} - A_{18})/4$  and  $\bar{B} = (B_{00} - B_{06} + B_{12} - B_{18})/4$ . This subtraction removes most of the sampling variability in the regression maps associated with atmospheric fluctuations with time scales longer than a day.

We have used a pure sinusoidal reference time series for the regression analysis, whereas the actual length of a lunar day varies over the lunar month and over the calendar year by up to half an hour [Lindzen and Chapman, 1969]. Hence, strictly speaking, our reference time series is based on the position of “mean Moon,” rather than that of the actual Moon. This approximation results in a damping of the tidal signal that we seek to isolate. However, we confirmed that the cumulative deviation of the Moon’s phase from the mean Moon phase does not exceed 1 day. Hence, the use of the mean lunar synodic cycle in this study should be suitable for purposes of detection.

### 3. Detection of $L2$ in the TRMM Data

Figure 1 (top row) shows  $\bar{A}$  and  $\bar{B}$  for mass-weighted vertical mean geopotential height and divergence over the tropical troposphere (i.e., 1000–100 hPa) from the ERA-Interim reanalysis data. In agreement with the classical view of tides, high-pressure tide is observed when the mean Moon is overhead (i.e., mean lunar transit) and underfoot, so that zonal wave number 2 patterns emerge on a global map. The perturbations in pressure and divergence are in quadrature. Consistent with tidal theory, locations experiencing the maximum divergence at given time will experience lowest pressure (and therefore lowest temperature) tides 3 h later and vice versa.

The color shading in Figure 1 (bottom row) shows the corresponding patterns for  $P$  in the TRMM data. Because the time resolution of the TRMM data set is three hourly, we have extended the definition of  $\bar{A}$  and  $\bar{B}$  as  $\bar{A} = (A_{00} - A_{06} + A_{12} - A_{18} + B_{03} - B_{09} + B_{15} - B_{21})/8$  and  $\bar{B} = (B_{00} - B_{06} + B_{12} - B_{18} - A_{03} + A_{09} - A_{15} + A_{21})/8$  by adding data at 03, 09, 15, and 21 UTC to increase the statistical degrees of freedom. The patterns are noisy, but there is a hint of a zonal wave number 2 signature, out of phase with the more clearly defined pressure signature.

To obtain a clearer picture of  $L2$ , we have also performed a compositing analysis by superposing all the four positive antinodes in  $\bar{A}$  and  $\bar{B}$  at the same locations. We note that this operation places the four negative antinodes at the same locations as well. Figure 2 (left column) shows the composite maps, which exhibit a

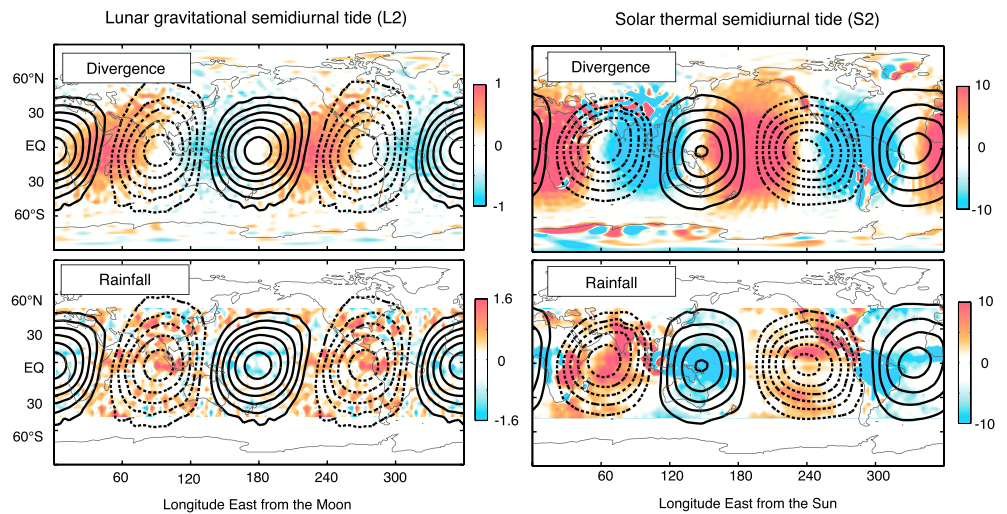


**Figure 2.** (left column) As in Figure 1 (left column) but composited so that all the four positive antinodes in  $\bar{A}$  and  $\bar{B}$  are superimposed at the same location. Maps are repeated once in the longitudinal direction. The coastlines are for the time when the Moon is above the Greenwich Meridian. (right column) As in Figure 2 (left column) but for the solar semidiurnal tide estimated by compositing the fields for each time of day and then subtracting as (00 UTC 06 UTC + 12 UTC 18 UTC)/4. Contour interval 2 m.

clearer correspondence between pressure and  $P$  than the patterns shown in Figure 1. As suggested in previous studies [Haurwitz and Cowley, 1969; Lindzen and Chapman, 1969], the phase of L2 in pressure and divergence field is slightly earlier in Southern Hemisphere.

For comparison, we also show the patterns of solar semidiurnal tide (S2) (Figure 2, right column). The climatology of S2 at each time of day is calculated as the average of each  $x_i$  over the full time span of the data, rather than as a regression coefficient based on a sinusoidal reference time series. As in L2, horizontal divergence is quadrature with pressure, and “high tide” (defined in terms of pressure or geopotential height) corresponds to reduced  $P$  and vice versa.

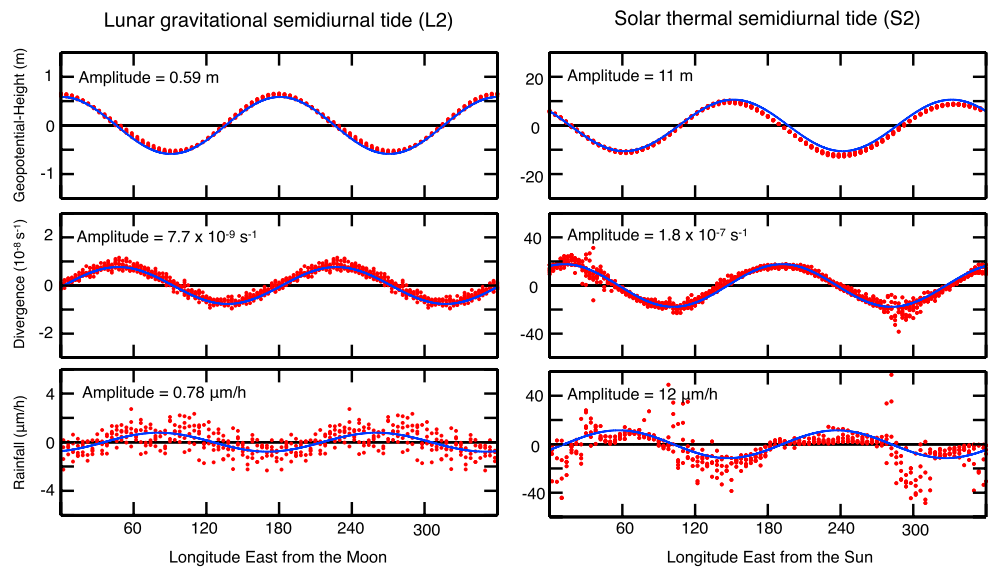


**Figure 3.** As in Figure 2 but scatterplots showing the data at each grid point from 10°S to 10°N by binning by 4.5° longitude increments. Also shown are sinusoidal least squares best fit curves for zonal wave number 2. Amplitudes of the curves are indicated at the top left of each panel.

**Table 1.** Estimated Tidal Amplitude in the Tropics

Variables (Unit)	L2	S2
Geopotential height (m)	0.59	11
Temperature (barotropic) (mK)	5.8	108
Temperature (baroclinic) (mK)	1.6	-
Temperature (total) (mK)	7.4	108
Relative humidity (%)	0.039	0.56
Precipitation rate ( $\mu\text{m}/\text{h}$ )	0.78	12

To determine the tidal amplitude objectively, we have performed harmonic analysis as a function of longitude. Figure 3 shows scatterplots for each variable in both L2 and S2 produced by partitioning the data between  $10^\circ\text{S}$  and  $10^\circ\text{N}$  into longitudinal bins. Also shown are sinusoidal least squares best fit curves for zonal wave number 2. Estimated tidal amplitude is printed in the top left corner of each panel. It is notable that the L2

modulation in  $P$  is only on the order of  $1 \mu\text{m}/\text{h}$  yet is clearly detectable. The amplitude determined by this method also suggests that the tidal amplitudes of pressure, divergence, and  $P$  in L2 are about 20 times smaller than in S2. For reference, *Forbes et al.* [1997] estimated, based on an earlier satellite-based rainfall product, that the “migrating (Sun-synchronous)” S2 component near the equator exhibits an amplitude of  $\sim 0.6 \text{ mm}/\text{d}$ , which is about twice as large as the value that we have obtained from TRMM (i.e.,  $10 \mu\text{m}/\text{h}$  or  $0.24 \text{ mm}/\text{d}$ ).

#### 4. Implications for the Relationship Between Tropical Relative Humidity and Precipitation Rate

We have estimated tropospheric temperature changes on height surfaces ( $dT$ ) that occur in response to the pressure changes in L2 and S2, taking into account both the barotropic component that exists in the absence of any temperature changes on pressure surfaces and the baroclinic component associated with vertical gradients of tidal amplitude and phase. Because the barotropic component of  $dT$  does not involve thickness anomalies, it can be calculated from  $\bar{A}$  and  $\bar{B}$  of mass-weighted vertical mean geopotential height, assuming that the process is adiabatic and hydrostatic. We have obtained the baroclinic  $dT$  by analyzing mass-weighted vertical mean temperature within 1000–100 hPa: geographical distributions of  $\bar{A}$  and  $\bar{B}$  are shown in Figure S1 in the supporting information, which exhibit clear zonal wave number 2 patterns. For L2, the baroclinic contribution to the temperature signal is  $\sim 30\%$  as large as the barotropic contribution; for S2, the baroclinic contribution is negligible. To infer the corresponding changes in RH, we use the linearized Clausius-Clapeyron

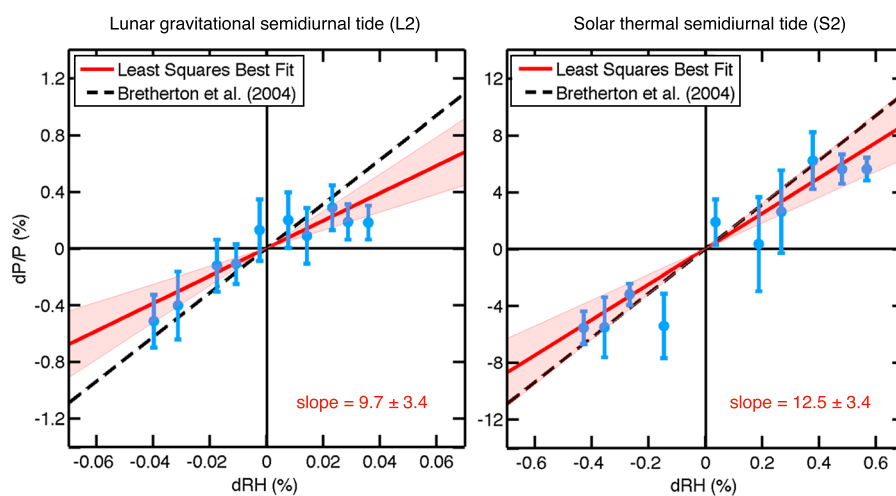


**Figure 4.** Relationships between relative humidity change ( $dRH$ ) estimated as described in the text and percentage change of precipitation rate ( $dP/P$ ) associated with the (left) lunar and (right) solar semidiurnal tide in regional ( $22.5^\circ$  in longitude by  $4.5^\circ$  in latitude) bins in the tropical domain  $30^\circ\text{S}$ – $30^\circ\text{N}$ . The blue symbols show composites of  $dP/P$  for  $dRH$  bins by 10 percentile increments, and the error bars correspond to 2 standard deviations. Red lines are the least squares best fit of the composites under the constraint that the lines cross the origin (i.e.,  $dRH = dP/P = 0$ ), and the shaded areas show their estimated uncertainties at the 95% confidence level. Also shown as black dashed lines are estimates by *Bretherton et al.* [2004], who investigated the same relationship but in natural day-to-day variability.

equation, i.e.,  $de_s/e_s = (0.074/K)dT$ , where  $e_s$  is the saturation vapor pressure. Assuming that the specific humidity change is negligible on the semidiurnal time scale,  $dRH/RH = -de_s/e_s$ . Then, to calculate  $dRH$ , we assume that the effective vertically averaged RH is 70%. Typical tidal amplitudes in the tropics are summarized in Table 1.

Figure 4 shows the relationship between  $dRH$  and logarithmic changes in  $P$ , i.e.,  $dP/P$ , induced by  $L2$  and  $S2$ . Our results indicate that a 1% increase in RH causes  $P$  to increase by  $\sim 10\%$  in  $L2$  and  $\sim 12\%$  in  $S2$ . Also shown is an estimate by Bretherton *et al.* [2004] who investigated the same relationship between  $P$  and column RH in natural day-to-day variability. They obtained the column RH by dividing the observed water vapor path based on satellite measurements by the corresponding saturation water vapor path at each grid point and performed a nonlinear least squares analysis for oceanic basin-wide regional bins. They estimated an  $\sim 16\%$   $P$  increase for a 1% RH increase. Those values obtained using these different approaches agree as well as they do support the notion that  $P$  is highly sensitive to small changes in the ambient RH under the current tropical climate condition.

## 5. Concluding Remarks

In both KW14 and the present study, we have analyzed the  $S2$  as well as the  $L2$  tidal signals. We have placed greater emphasis on findings related to  $L2$  in these papers because of their greater novelty and because the  $L2$  forcing is purely adiabatic. The  $S2$  forcing involves diabatic heating, in the ozone layer and at the Earth's surface. That the  $S2$  pressure tide shown in Figure 2 exhibits a tropically focused zonal wave number 2 signature indicates that it is forced mainly by ozone heating. That the tropospheric signal is almost pure barotropic (KW14, Figure 3) confirms that it is a passive response to diabatic heating at much higher levels of the atmosphere. In contrast to the  $L2$  pressure signature, which may be distorted by irregular features of the oceanic tide [Schindelegger and Dobsław, 2016], the  $S2$  pressure signature is much closer to a pure, equatorially symmetric, zonal wave number 2 pattern.

In agreement with previous studies, we find that the amplitude of the  $S2$  pressure signature induced by ozone heating is about 20 times as large as that of the  $L2$  signature induced by perturbations in the gravitational field. We have shown that this scaling applies to  $P$  as well. Hence, for some sensitivity studies such as the present one, the  $S2$  and  $L2$  signatures can be used interchangeably. However, it is evident from Figure 2 that the  $S2$  signature in  $P$  exhibits pronounced, boundary-forced land-sea contrasts. The  $S2$  temperature signature (not shown) exhibits even more substantial departures from the zonal wave number 2 pattern predicted by classical tidal theory. These features complicate the interpretation of relationships derived exclusively from the  $S2$  signal.

The analysis of the relationship between relative humidity and  $dP/P$  in section 4 serves as a concrete illustration of how the quantitative documentation of the observed structure of atmospheric tides can be used to make inferences about atmospheric processes. It can also serve as a test bed for evaluating and comparing the performance of models.

### Acknowledgments

This study is based on the TRMM data set available online at <http://pmm.nasa.gov/data-access/downloads/trmm> and the ERA-Interim data set available at <http://apps.ecmwf.int/datasets/data/interim-full-daily>. The work was supported by the National Science Foundation (NSF) under grant AGS-1122989, and the first author's graduate work is supported by Takenaka Ikueikai Scholarship Society, Iizuka Takeshi Scholarship Foundation, and the NSF under grant AGS-0960497. We would like to thank Katrina Virts for preprocessing the TRMM data. We would also like to thank Christopher Bretherton, Michael Schindelegger, Kevin Hamilton, and one anonymous reviewer for their helpful comments and suggestions.

### References

- Bretherton, C. S., M. E. Peters, and L. E. Back (2004), Relationships between water vapor path and precipitation over the tropical oceans, *J. Clim.*, *17*, 1517–1528, doi:10.1175/1520-0442(2004)017<1517:RBWVPA>2.0.CO;2.
- Chapman, S. (1951), Atmospheric tides and oscillations, in *Compendium of Meteorology*, edited by T. F. Malone, pp. 262–274, Am. Meteorol. Soc., Boston, Calif.
- Dee, D. P., et al. (2011), The ERA-Interim reanalysis: Configuration and performance of the data assimilation system, *Q. J. R. Meteorol. Soc.*, *137*, 553–597, doi:10.1002/qj.828.
- Forbes, J. M., M. E. Hagan, X. Zhang, and K. Hamilton (1997), Upper atmosphere tidal oscillations due to latent heat release in the tropical troposphere, *Ann. Geophys.*, *15*(9), 1165–1175, doi:10.1007/s00585-997-1165-0.
- Goulter, S. W. (2005), The structure of the lunar semi-diurnal pressure tide  $L2$ , *Q. J. R. Meteorol. Soc.*, *131*, 723–758, doi:10.1256/qj.03.234.
- Haurwitz, B., and A. D. Cowley (1969), The lunar barometric tide, its global distribution and annual variation, *Pure Appl. Geophys.*, *75*, 1–29, doi:10.1007/BF00876008.
- Huffman, G. J., D. T. Bolvin, E. J. Nelkin, D. B. Wolff, R. F. Adler, G. Gu, Y. Hong, K. P. Bowman, and E. F. Stocker (2007), The TRMM multi-satellite precipitation analysis: Quasi-global, multi-year, combined-sensor precipitation estimates at fine scale, *J. Hydrometeorol.*, *8*(1), 38–55, doi:10.1175/JHM560.1.
- Kohyama, T., and J. M. Wallace (2014), Lunar gravitational atmospheric tide, surface to 50 km in a global, gridded data set, *Geophys. Res. Lett.*, *41*, 8660–8665, doi:10.1002/2014GL060818.
- Lindzen, R. S., and S. Chapman (1969), Atmospheric tides, *Space Sci. Rev.*, *10*, 3–188.
- Schindelegger, M., and H. Dobsław (2016), A global ground truth view of the lunar air pressure tide  $L2$ , *J. Geophys. Res. Atmos.*, *120*, doi:10.1002/2015JD024243.